Morphology, thermal properties and crystallization kinetics of ternary blends of the polylactide and starch biopolymers and nanoclay: The role of nanoclay hydrophobicity

Obiro Cuthbert Wokadala[a,b], Suprakas Sinha Ray[a,b*], Jayita Bandyopadhyay[a], James Wesley-Smith[a], Naushad Mohammad Emmambux[c]

[a]*DST/CSIR National Centre for Nanostructured Materials, Council for Scientific and Industrial Research, 1-Meiring Naude Road, Brummeria, Pretoria 0001, South Africa*

[b]*Department of Applied Chemistry, University of Johannesburg, Doornfontein 2028, Johannesburg, South Africa*

[c]*Department of Food Science, University of Pretoria, Pretoria 0001, South Africa*

*Corresponding author. Fax: +27 12 841 2229; e-mail: rsuprakas@csir.co.za

ABSTRACT: Polylactide/butylated-starch/nanoclay (70/25.5/4.5 wt%) composites were prepared by melt blending with nanoclays of varying hydrophobicity. Electron microscopy studies indicated that the interphase boundary interaction was highest in the clay with intermediate hydrophobicity but decreased with clays of higher or lower hydrophobicity. Conventional and modulated differential scanning calorimetry studies showed that, in the case of composites, the change in the ratio of rigid and mobile amorphous fractions depends on the hydrophobicity of clays used for the preparation of blend composites. The mobile amorphous fraction related to the polylactide phase decreases in the case of intermediate hydrophobic clay compared with less and more hydrophobic clays or neat blend samples. Avrami bulk crystallization analysis and polarized optical microscopic observation demonstrated that hydrophobic clays hindered the crystallization of the PLA phase into the formation of disc-shaped spherulites. On the basis of obtained results, we propose a general understanding on how the morphology and thermal properties of the blend composites are related to the hydrophobicity of the nanoclays.

KEYWORDS: polylactide/butylated-starch blend; nanoclay hydrophobicity; morphology, thermal properties and crystallization kinetics

1. Introduction

Polylactide (PLA) is a widely researched biodegradable biopolymer that has been used successfully to develop several commercial products in the health, food and pharmaceutical industries [1, 2]. Over the last few years, research has been undertaken to incorporate less expensive and more readily available, nature-derived polymeric materials, such as starch, into PLA. Starch is the most abundant [3] inexpensive biopolymer, but attempts to incorporate it into PLA have been challenging due to its granularity and the hydrophilic nature conferred by hydroxyl-groups on the glucose backbone [4]. PLA-starch compatibility has been increased by hydrophobic modification of starch [5] and by using cross-linkers and/or a compatibilizers such as maleic anhydride [6-8]. However, even with such modifications, the amount of starch added to the blend cannot exceed approximately 20 wt% without adversely affecting the properties of PLA [5].

A significant amount of research has shown that the incorporation of organically modified clays (organoclay) into ternary blends improves the interfacial compatibility of the immiscible polymers and the resultant mechanical and thermal properties [9-13]. The surfactants in the nanoclay are proposed to reduce the interfacial tension between the inter-silicate layer space and the polymer chains, hence facilitating the penetration of the chains into the two-dimensional silicate gallery [9]. In the case of organoclay-containing immiscible polymer blends, there could be preferential localization of the intercalated silicate layers in either of the two polymers [14, 15], which eventually affects the thermal and mechanical properties of blend composites. The preferential localization is mainly driven by two factors: (i) thermodynamic (such as enthalpic interaction between each polymer and the clay particles) and (ii) kinetic factors (e.g., viscosity ratios of the two polymers). Wu et al. [15] reported the effect of localization of silicate layers and carbon

nanotubes (CNTs) on the morphology and crystallization of PLA/poly(ε-caprolactone) (PCL) blends. The transmission electron microscopy (TEM) results [16] indicated that the intercalated silicate layers were selectively located in the PLA phase and at the interface due to enthalpic interactions between the two, whereas the CNTs were mainly found in the PCL and at the interface. However, with reduced viscosity ratio of the blend matrix, the CNTs changed their preferred location from PCL to PLA, signifying an interplay of both thermodynamic and kinetic aspects, in the determination of the preferred localization of CNTs. Similarly, Chen and co-workers [16, 17] compared the influence of organoclay and twice functionalized clay on the morphology and properties of PLA/poly(butylene succinate) (PBS) and PLA/poly(butylene succinate-*co*-butylene adipate) (PBSA) blends. Recently, As'habi et al. [18] studied the effect of mixing sequences and organoclay types on the morphological, rheological and degradation behavior of PLA/low density polyethylene (LLDPE) nanocomposites. The PLA/LLDPE/clay nanocomposites were prepared using two commercially available organically modified montmorillonite (OMMT): Cloisite®30B (C30B) and Cloisite®15A (C15A). The results showed that, in comparison to C15A, C30B had strong influence on the reduction of dispersed LLDPE phase and C30B particles were highly delaminated in the PLA phase. The authors also found that some delaminated clay particles were located at the interphase, but no localization of clay particles was observed in the LLDPE matrix when C15A was used for nanocomposite formation. They also found that mixing-sequences had no effect on clay particles localization. In our previous reports [19-21], pristine clay and four organoclays were investigated for their ability to influence the morphology and hence the properties of the PLA/PBSA blend. The clay interlayer spacing, the concentration of the modifier on the clay surface and the miscibility between the polymers and the surfactant were found to influence the resulting morphology and hence the properties.

Research investigating nanoclay-containing polymer blend composites has focused mainly on systems with two hydrophobic polymers, biopolymers or biodegradable polymers, with little

consideration for systems in which one biopolymer is significantly less hydrophobic than the other. Such ternary systems would involve natural biopolymers, such as starch, zein, gluten and kafirins, which generally are not entirely hydrophobic, even after hydrophobic modification [5]. Recently, research on starch has shown that hydrophobically modified starch preferably interacts with organoclays that have intermediate-hydrophobicity rather than clays with relatively low and high hydrophobicity [22]. The hydrophobicity of a given nanoclay would therefore probably affect the properties of ternary biopolymer blend composites. Therefore, the present study was conducted to investigate the effect of clays' hydrophobicity on the morphology/structural, thermal and crystallization behavior of PLA/butylated starch blend composites.

2. Experimental methods

2.1. Materials

The PLA was a commercial grade PLA 2002D® (Natureworks LLC, USA) with M_w = 235 kg/mol, a *D*-isomer percentage of approximately 4% and a density of 1.24 g/cm^3. The glass transition and melting temperatures of the PLA were 60°C and 153°C, respectively. The melt-complex viscosity of neat PLA was 1000 Pa.s, measured at 185°C and a strain of 0.2%. Normal maize starch (S4126, with approximately 70% amylopectin) was obtained from Sigma-Aldrich, South Africa. Butylene oxide (1, 2-epoxybutane), sodium hydroxide, sodium sulfate and other chemicals were of analytical grade and were obtained from Merck, South Africa. The pristine clay and various organoclays utilized in this study were obtained from Southern Clay Products, USA, and their characteristics were as summarized in Table 1.

2.2. Processing of PLA/butylated starch blend and blend/clay composites

Butyl-etherification of starch was performed according to Bien et al. [23] with our own modifications using a Parr-stirred reactor (Parr Instrument Company, USA) [5]. The molar ratio of both sodium hydroxide and sulfate to starch was 1:2, while the molar ratio of butylene oxide to

starch (as glucose) was 1:7. The reaction material was heated at 140°C with a stirring at 250 rpm for 100 min in a closed reactor. The resultant material was neutralized with 1 M HCl, washed 20 times with excess water and then vacuum dried at 80°C for 5 days to obtain the butylated starch material. The degree of molecular substitution (D.S) of the resultant butylated starch was approximately 2. The D.S was determined according to Wokadala et al. [5] using a Varian Mercury 400 MHz NMR spectrometer (Varian Mercury, USA). This starch can be considered to have good hydrophobicity due to replacement of approximately two-thirds of the hydrophilic hydroxyl groups in the glucose monomers of the starch [5]. The melt-complex viscosity of modified starch was 400 Pa.s, measured at 185°C and a strain of 0.2%.

Table 1. Physical characteristics of pristine and organoclay used in this research.

Commercial name	Organic modifier*	Modifier concentration (meq/100 gm)**	$d_{(001)}$ spacing (nm)	Solubility factors (δ) ($J^{1/2}.cm^{-3/2}$)***	Polarity
Cloisite® Na (CNA)	none	CEC= 92.6	1.17	–	Highly hydrophilic
Cloisite®30B (C30B)	Methyl tallow bis-2-hydroxyethyl quaternary ammonium	90	1.85	21.5	Less hydrophobic
Cloisite®10A (C10A)	Dimethyl benzyl hydrogenated tallow quaternary ammonium	125	1.92	19.1	Moderately hydrophobic
Cloisite® 93A (C93A)	Methyl dehydrogenated tallow ammonium	90	2.36	17.2	Hydrophobic
Cloisite® 20A (C20A)	Dimethyl dehydrogenated tallow quaternary ammonium	95	2.42	16.8	Very hydrophobic
Cloisite® 15A (C15A)	Dimethyl dehydrogenated tallow quaternary ammonium	125	3.15	16.8	Extremely hydrophobic

*The difference between C20A and C15A is that the first is washed and the latter is unwashed. Otherwise, both organoclays have the same surfactant. **CEC, cation exchange capacity. Modifier concentration, meq/100 g = milli equivalents of charge exchanged per 100 g mass of the pristine clay, here MMT. One meq/g is 96.5 Coulombs/g. ***Hydrophilic/hydrophobic descriptor levels are arbitrary and only relative in the table. Solubility factor of the surfactants were roughly calculated on the basis of the group contribution method of Fedor [24]. Additionally, we calculated on the basis of the expansion of gallery height when dispersed in ethanol.

The pristine clay and organoclay-containing PLA/butylated starch blend composites were prepared through melt blending using a HAAKE PolyLab OS Rheomix (Thermo Electron Co., USA) at 165°C for 10 min with a rotor speed of 80 rpm. The butylated starch, clays (pristine and modified)

and PLA were added at 25.5, 4.5 and 70 wt% of the total composite blend, respectively. The control sample was prepared without added clay and was abbreviated as PLA-ST-0. PLA-ST blend composites processed with CNA, C30B, C10A, C93A, C20A and C15A were correspondingly abbreviated as PLA-ST-CNA, PLA-ST-C30B, PLA-ST-C10A, PLA-ST-C93A, PLA-ST-C20A and PLA-ST-C15A. The resultant blend and blend/clay composites were then compression molded to the desired dimensions for the various tests using a Carver compression mold (Carver, USA). A total compression residence time of 10 min with a compression step of 2 min at a pressure of 2 metric ton was used.

3. Characterization

3.1. X-ray diffraction

The X-ray diffraction (XRD) patterns of the PLA/butylated starch/clay composites with the pristine clay and different organoclays were determined using a PANalytical X'pertPRO diffractometer (PANalytical, the Netherlands) (Cu Kα radiation; $\lambda = 0.154$ nm) with an operating voltage of 45 kV and current of 40 mA. The scanning was performed from $2\theta = 1°$ to 70° with a scanning step size of 0.0263° and a step time of 647.19 s.

3.2. Electron microscopy studies

The internal structure of the PLA/butylated starch blend and blend/clay composites was observed using a high resolution TEM (JEOL 2100 HRTEM, JEOL, Japan). Sections were obtained by cryo-sectioning at −120°C and a cutting speed of 0.08 mm/s using a Leica EM UC6 ultramicrotome (Austria) and a Diatome 35° diamond knife (Diatome, Switzerland). Sections of approximately 70 nm were obtained and mounted on 300 mesh copper grids for viewing. The images obtained were assessed using Digital Micrograph® software (Gatan, USA). To enhance the contrast between the phases, the sections were stained by osmium tetra-oxide, OsO_4 (5%), vapor.

The fractured-surface morphology of the PLA/butylated starch blend and blend/clay composites with different clay types was determined using a JEOL model JSM-7500F field emission scanning electron microscopy (SEM) (JEOL, Japan). An accelerating voltage of 3 kV was used under the gentle-beam-low mode to prevent the beam from damaging the sample. The samples were prepared by immersing in liquid nitrogen, cryo-fractured, allowed to warm, mounted on stubs edge-on and coated with carbon to enhance conductivity. The size of distinct features in the images was determined using ImageJ software (National Institutes of Health, USA).

3.3. Differential scanning calorimetry (DSC)

Three DSC experiment profiles were applied to study the thermal properties of the PLA/butylated starch blend and blend/clay composites. The first involved a conventional scan, where the samples (approximately 5 mg) were heated from 0-200°C and then held at 200°C for 5 min to destroy the previous thermal history. They were then cooled to 0°C and heated back to 200°C. Both the heating and cooling steps were performed at 10°C /min.

The mobile amorphous (W_{af}) and rigid amorphous (W_{raf}) phase fractions of the PLA/butylated starch blend and blend/clay composites were determined by applying a profile with both a conventional and a modulated heating ramp. Initially, the samples (10.2-10.8 mg) were heated with a conventional heating ramp from 0°C to 200°C at a rate of 15°C/min, held for 5 min to destroy the previous thermal history and then cooled at 15°C/min to 0°C. The samples were then heated with a modulated temperature ramp of 3.5°C/min, with an amplitude of ± 0.80°C and a period of 40 s. The mobile and rigid amorphous phase proportions in the PLA/butylated starch/clay composites were determined based on Righetti et al. [25] using Equations (1) and (2).

$$W_{af} = \frac{C_p}{C_{p100\%}} \quad \text{.....(1)}$$

$$W_{raf} = 1 - \frac{wt\%\ nanoclay}{100} - W_{af} \quad \text{.....(2)}$$

where X_c is the crystallized phase proportion at melting, ΔH_{mnr} is the melting enthalpy for crystalline from the non-reversing heat flow, ΔH_{mr} is the melting enthalpy from the reversing heat

flow, ΔH_{PLA} is the standard enthalpy of the completely crystalline PLA (93 J/g) [26], and C_p and $C_{p100\%}$ are the heat capacities of the samples and completely amorphous PLA, respectively. $C_{p100\%}$ was taken as 0.682 $J.g^{-1}.°C$ [27, 28].

An isothermal DSC scan profile was used to determine the crystallization kinetics of the PLA/butylated starch blend and blend/clay composites. In this profile, the samples (approximately 5 mg) were heated from 0° to 200°C at a rate of 10°C/min and then held for 5 min. The samples were then equilibrated to 120°C and held isothermally for 10 h for each sample. The heat flow rate of the sample was recorded until the baseline was recovered. The kinetics of the isothermal crystallization of the blend and blend/clay composite samples were then assessed using the Avrami bulk crystallization kinetics [29–31].

3.4. Polarized optical microscopy (POM)

The rate of PLA spherulite growth in the PLA/butylated starch blend and blend/clay composites was determined using a Carl Zeiss Imager microscope (Carl Zeiss, Germany) fitted with polarizing filters and a Linkam THMS heating stage (model CI 94, Linkam Scientific Instruments, Ltd., UK). The samples (approximately 50 μm thick) were placed between two glass cover slips. The temperature was then ramped to 200°C at a rate of 10°/min and held at 200°C for 5 min to destroy the thermal history. They were then equilibrated to 120°C and held at 120°C for up to 4 h. Images were recorded every 4 min using a charged couple device (CCD) camera. The rate of spherulite growth (G) was determined as the gradient of the linearly fitted data of the spherulite radius over time.

4. Results and discussion

4.1. Structure and morphology

Fig. 1 shows the XRD patterns of the compression molded PLA-ST composites with clays of different hydrophobicity. Fig. 1(a) shows the XRD patterns of pure CNA powder and PLA-ST-

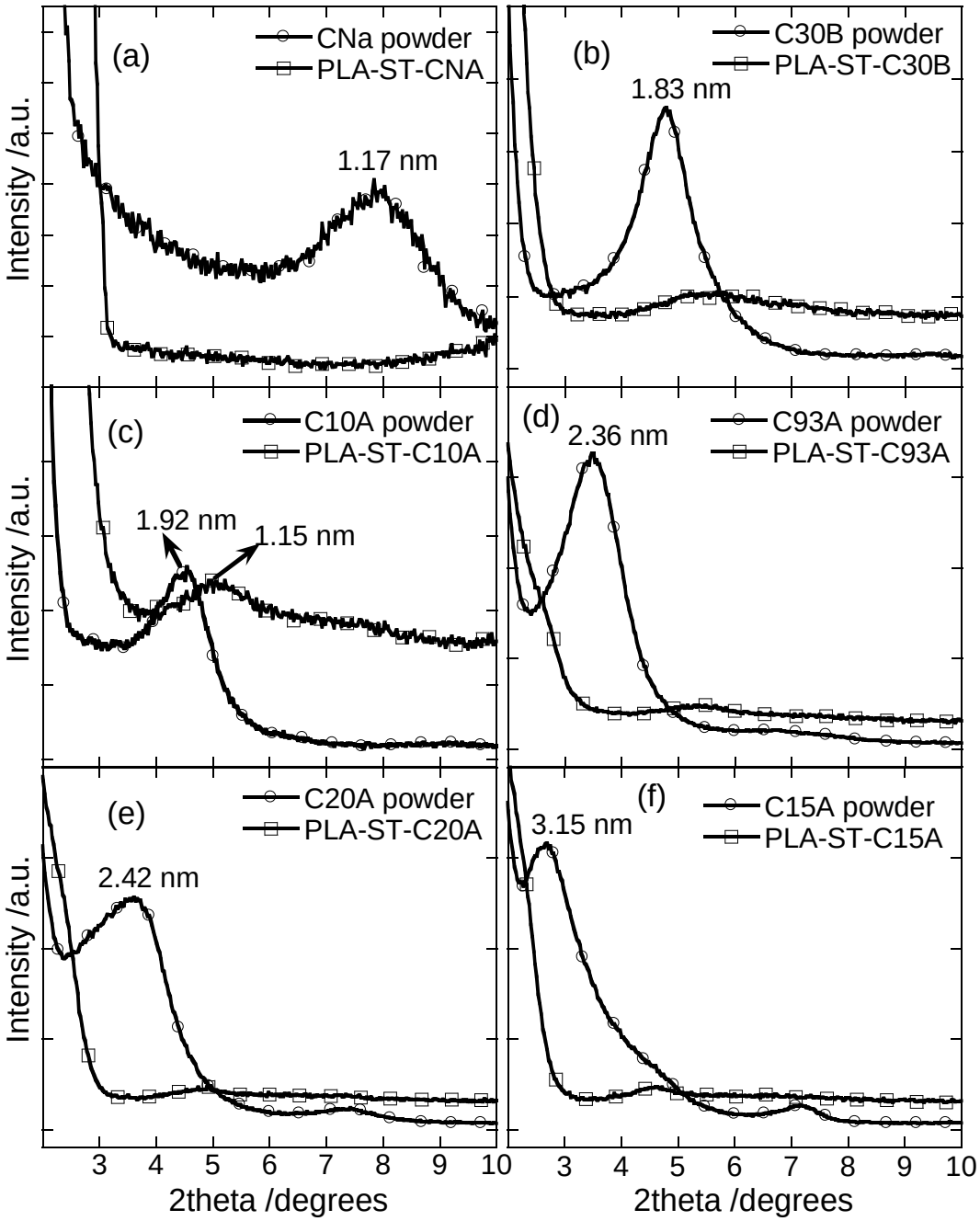

Fig. 1. XRD diffraction patterns of (a) pure CNA powder and PLA-ST-CNA, (b) pure C30B powder and PLA-ST-C30B, (c) pure C10A powder and PLA-ST-C10A, (d) pure C93A powder and PLA-ST-C93A, (e) pure C20A powder and PLA-ST-C20A and (f) pure C15A powder and PLA-ST-C15A.

CNA composite in the range of $2\theta = 2-10°$. The characteristic CNA (001) peak appeared at $2\theta =$ 7.94°. The XRD pattern of the PLA-ST-CNA composite was completely featureless, indicating a

high level of delamination of silicate layers in the blend matrix. Similar to PLA-ST-CNA, the XRD pattern of PLA-ST-C30B was also featureless within 2θ = 2−5°, but a broad and weak reflection peak appeared at 2θ = 5.47°. On the other hand, in the case of the PLA-ST-C10A composite, a sharp peak appeared at 2θ = 5° with a featureless diffraction pattern below 2θ = 5°.

+

On the other hand, PLA-ST-clay composites prepared with hydrophobic [C93A, Fig. 1(d)], very hydrophobic [C20A, Fig. 1(e)] and extremely hydrophobic [C15A, Fig. 1(f)] clays showed almost featureless diffraction patterns associated with a high-angle weak reflection peak in their respective XRD patterns. Therefore, on the basis of XRD patterns of various composites, it is very difficult to make any conclusion about the degree of dispersion of silicate layers in the blend matrix. One reason for this type of observation is the orientation of silicate layers in different plane as we conducted XRD measurements in reflection mode [32]. The intercalate composition or silicate concentration in composites may also contribute to the featureless XRD patterns [32]. Therefore, TEM will be the main tool to determine the fate of the dispersed silicate layers in the PLA-ST blend matrix because it allows a qualitative understanding of the internal structure, spatial distribution of the various phases and defect structure through direct visualization [33].

Fig. 2 shows the TEM images of the blend and blend composites prepared with clays of different hydrophobicity. In general, TEM images are not consistent with the XRD patterns. Fig. 2(a) is a bright field TEM image of PLA-ST-0 that gives a general view of the dispersed starch domain in the PLA matrix. The clays in all of the samples were mainly found in the butylated starch phase with the exception of the PLA-ST-C20A composite, where intercalated clay particles were dispersed in both phases and at the interphase. Given that the PLA is more hydrophobic than the butylated starch (D.S = 2), it would have been expected that at least for the extremely hydrophobic clay, such as C15A, with larger initial *d*-spacing (see Table 1) would be preferentially located in the PLA phase. However, because the clays are not entirely hydrophobic [33, 34], it is possible

that the relative interfacial tensions were higher with PLA compared with butylated starch, hence the location of intercalated silicate layers within the starch phase in most composites. An alternative explanation for the location of the clays in the starch phase could be based on a difference in the viscosity ratio between the butylated starch phase and the PLA phase. The viscosity ratio between two polymers greatly affects the level of mixing [15]. The intercalated silicate layers would preferentially locate in the starch phase because the starch phase had a much lower viscosity compared with the PLA phase (experimental section). This effect could have played a dominant role because even the most hydrophobic clays, i.e., the intercalated silicate layers, were only found in the starch phase rather than in the PLA phase. Another factor is the balance of the interlayer spacing of the clay and enthalpic interaction between blend components and the surfactants used in the modification of pristine MMT. This requirement may be satisfied with C20A and, for this reason, intercalated silicate layers are dispersed in both phases and at the interface. A similar type of observation has been made by Ray et al. [10, 20, 21] in the case of poly(methyl methacrylate) and polycarbonate [10] and PLA/PBSA blend systems [20, 21].

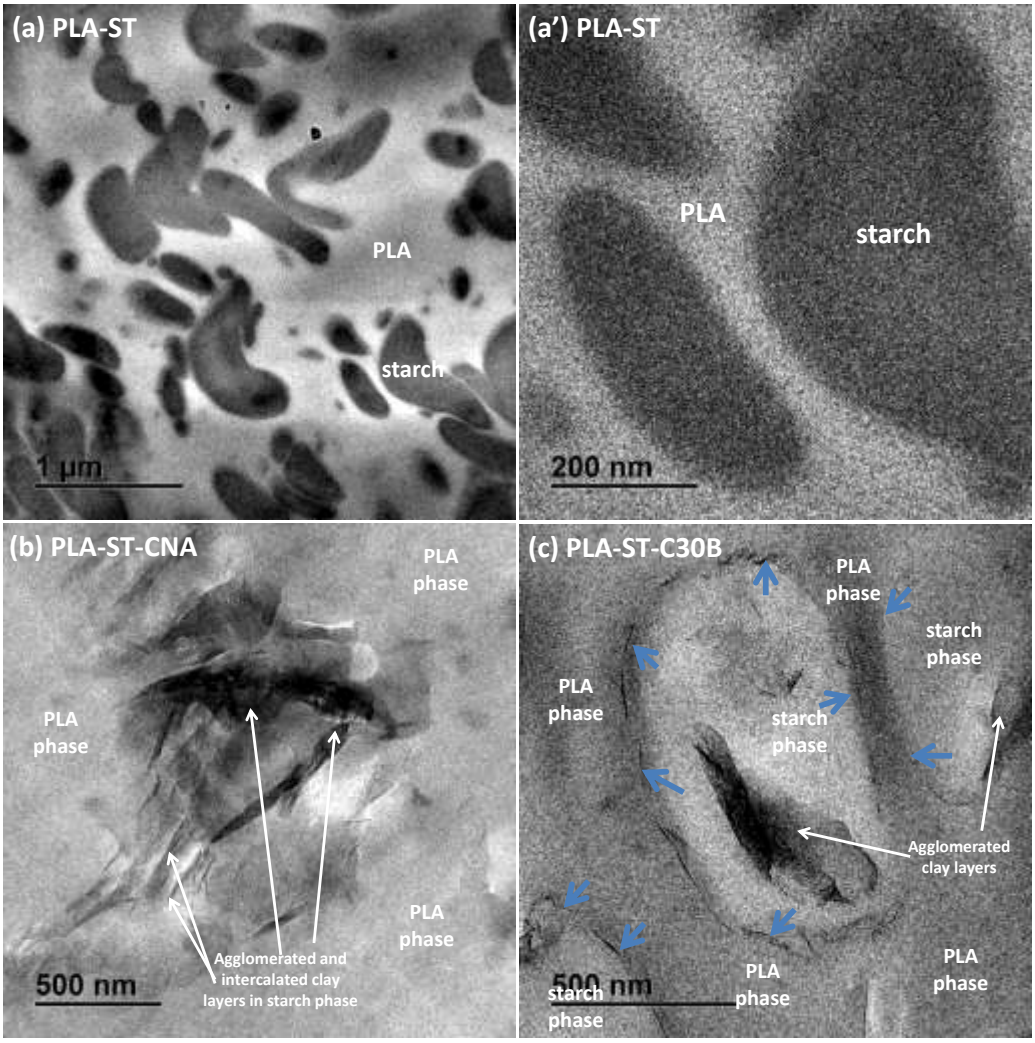

Fig. 2. Bright field TEM images of (a, a') PLA-ST blend at two different magnifications, (b) PLA-ST-CNA and (c) PLA-ST-C0B
composites. Arrows indicating the dispersion of silicate layers at different phases and at the interphase.

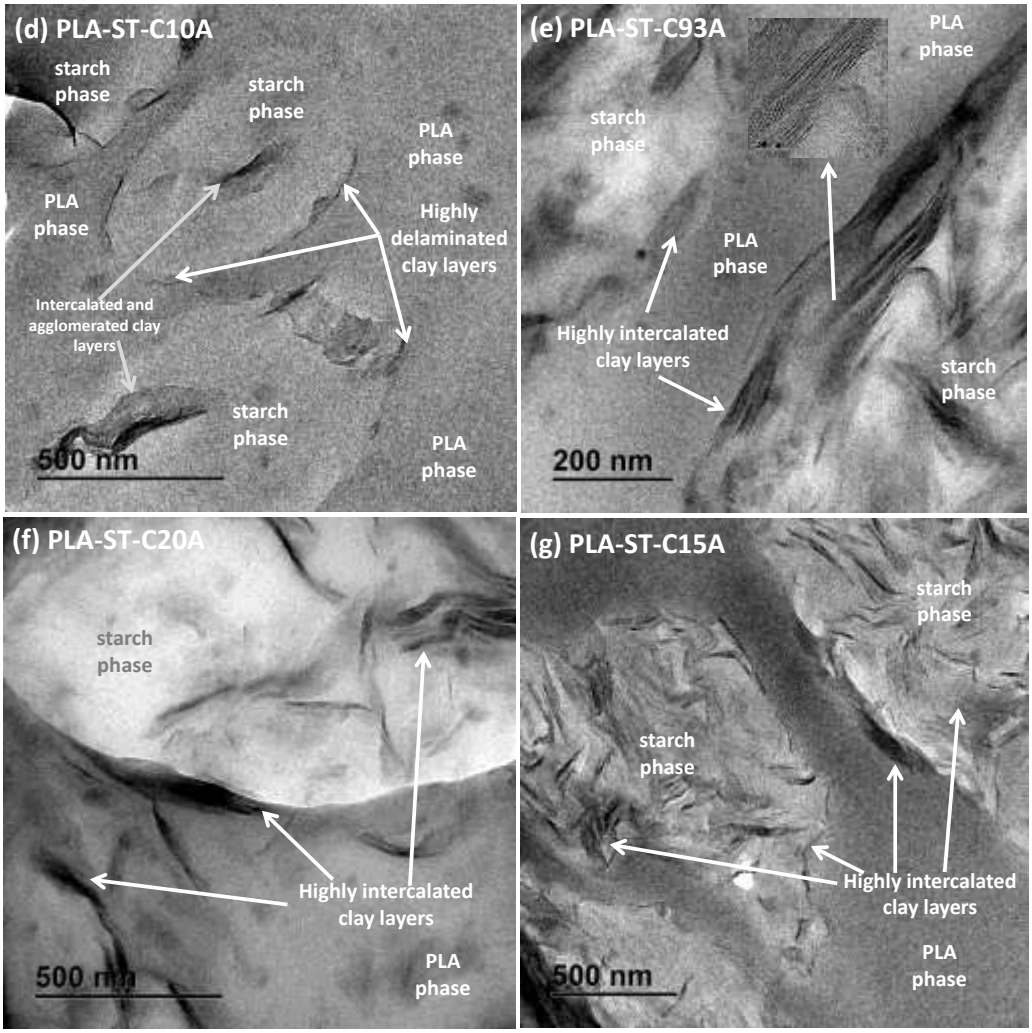

Fig. 2 (continued). Bright field TEM images of (d) PLA-ST-C10A, (e) PLA-ST-C93A and (f) PLA-ST-C20A and (g) PLA-ST-C15A composites. Arrows indicating the dispersion of silicate layers at different phases and at the interphase.

There was a difference in the structure of the dispersed silicate layers at the interphase boundary between the composites with clays of different hydrophobicity. In the case of the PLA-ST-CNA composite, it was difficult to differentiate the interphase boundary between two phases, and mostly agglomerated layers with few intercalated silicate were dispersed in the starch phase. This is due to the strong hydrophilic nature of CNA and poor interaction with the highly hydrophobic PLA phase. In the case of PLA-ST composites with less and moderately hydrophobic clays, such as C30B and C10A, stack and intercalated clay layers were dispersed in the starch phase, whereas highly delaminated silicate layers were moved to the interphase. In the case of PLA-ST-C93A and PLA-ST-C15A composites, silicate layers were also selectively dispersed in the starch phase and

at the interphase between starch and PLA matrices. On the other hand, in the case of the PLA-ST-C20A composite, highly intercalated silicate layers were dispersed in both phases and at the interphase. This may be linked to the nature of C20A, which has a balance of hydrophilicity/hydrophobicity and interlayer spacing [10, 19, 20].

Fig. 3 shows the SEM freeze-fractured images of PLA-ST blend and blend/clay composites with clays of different hydrophobicity. A phase-separated structure with a round to ovoid dispersed phase was observed in the blend without clay and the composites with added clays. In the case of the PLA-ST blend, the sizes of the dispersed phase were approximately 0.70 ± 0.25 μm. For the PLA-ST composites with CNA, C30B, C10A, C93A, C20A and C15A, the sizes of dispersed phases were approximately 0.56 ± 0.24, 1.09 ± 0.39, 1.46 ± 0.38, 1.30 ± 0.41, 1.29 ± 0.47 and 1.50 ± 0.70 μm, respectively.

In a mixture of immiscible polymers, the presence of anisotropic nanoparticles in one of the polymer phases has been suggested to affect the morphology and properties of the resultant composites based on a modification of the viscosity [15]. In the present research, given that the intercalated silicate layers were mostly located in the starch phase (from the TEM results), they were bound to affect the viscosity of the starch phase. The smallest sizes of the dispersed phase were observed more in the case of the PLA-ST-CNA composite than in the neat blend or other blend composites containing clays with different hydrophobicity. The observed smaller size of the dispersed phase could have resulted from an effect of the silicate layers on the viscosity ratio between the continuous PLA phase and the dispersed butylated starch phase. As we observed in the TEM image of PLA-ST-CNA [Fig. 2(b)], highly agglomerated silicate layers were dispersed in the starch phase, leading to the increase in viscosity ratio of the starch phase. Among all organoclays containing composites, such as the PLA-ST-C30B composite with less hydrophobic clay, smaller dispersed starch phases were observed. On the other hand, the sizes of the dispersed phase were almost similar in the case of PLA-ST-C10A and PLA-ST-C15A composites.

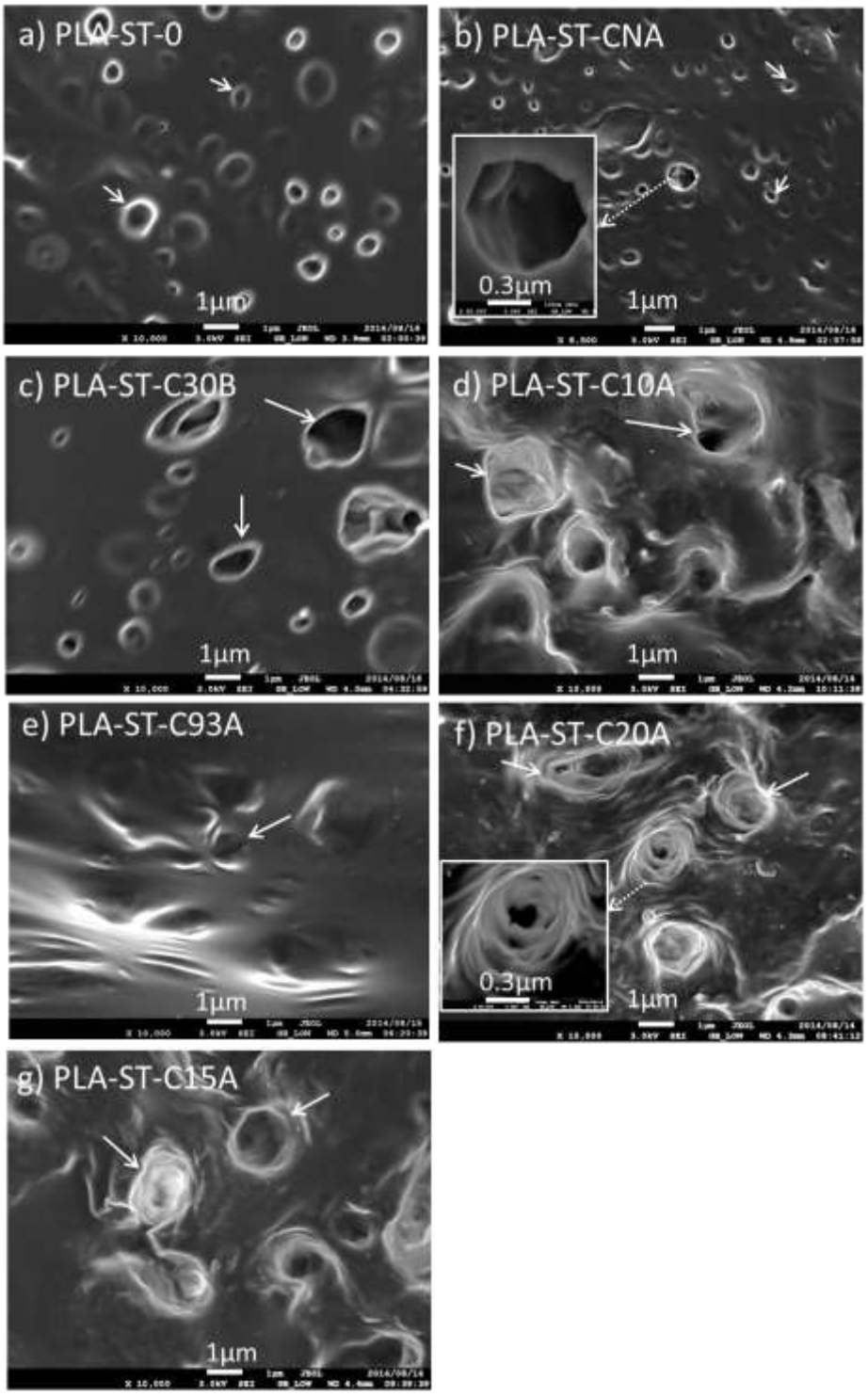

Fig. 3. Fractured surface-morphology PLA/butylated starch blend and blend/clay composites with clays of different degrees of hydrophobicity. The main images were collected at ×10,000, while the inset images (b and f) were collected at ×65,000 with a voltage of 3 kV.

Therefore, it can be concluded that the highly delaminated silicate layers at the interphase prevented the coalescing of the butylated starch phase, thereby leading to small, well-distributed

starch phases in the composite with C30B. On the other hand, larger dispersed phases, which are mostly embedded in the PLA matrix, were observed in the composites with more hydrophobic clays. As the level of butylated starch-nanoclay interaction with the more hydrophobic clays increased, the viscosity of the starch phase probably increased further, as evidenced by the increase in degree of intercalation of silicate layers in the starch phase, leading to a lower difference in viscosity between the starch and PLA phases. The reduced viscosity difference led to more interaction between the phases, and the coalescing of the butylated starch phase into the large distinct phases was observed.

Closer observation of the round to ovoid distinct phases at higher magnification [see insets in (b) and (f) of Fig. 3] showed that there was a difference in the structure between the distinct features in the composites with less hydrophobic systems (control, CNA, C30B, C10A) [see example in inset of Fig. 3(b)] and those with more hydrophobic systems (composites with C20A and C15A) [see inset of Fig. 3(f)]. The dispersed phase structures in the control sample and composites with less to moderate hydrophobic clays (Figs. 3a, b, c and d) had relatively distinct boundaries at which the discontinuous starch phase was clearly separated from the continuous PLA phase [see inset of Fig. 3(b)]. On the other hand, the boundary of the dispersed phase structures in the composites with very to extremely hydrophobic clays [C20A, C15A; parts (f) and (g) of Fig. 3) was less clearly separated from the continuous PLA phase and apparently consisted of concentric rings [see inset of Fig. 3(f)]. However, it was difficult to identify the boundary of the dispersed phase structures in the composite containing the hydrophobic clay, i.e., C93A [see Fig. 3(e)]. This implied that the interaction between the starch and PLA phase was most intimate in the composites with C93A, decreased in the composites with C20A and C15A and lowest in the composites with CNA, C30B and C10A. It can be inferred that, even in the presence of compatibilizing nanoclays, for enhanced compatibility at the micron scale, a match in hydrophobicity at the nanoscale

between the organic modifier and that of the dispersed phase is necessary to facilitate intimate interaction.

4.2. Thermal properties

Assessment of the thermal properties of the composites based on PLA would enable further understanding of the interaction between the PLA, butylated starch and nanoclays with different hydrophobicity. Fig. 4 shows the standard/conventional DSC curves of the neat blend and blend/clay composites. All of the samples showed a glass transition with enthalpy relaxation at approximately 55°C (see bold black arrow on top curve). There was some apparent cold crystallization for the samples that could not be clearly separated from the melting endotherm (see bold white arrow in Fig. 4). The melting endotherms appeared at approximately 150°C (Fig. 4), and the values could not be accurately determined because of the apparent influence of the cold crystallization exotherms. It was clear that the area under the cold crystallization and melting peaks (enthalpy of cold crystallization and melting, respectively) was higher for the control sample and the samples with less to moderate hydrophobic clays when compared with that of the composites with hydrophobic to extremely hydrophobic clays. This indicated a tendency of the more hydrophobic clays to hinder the re-arrangement of the PLA molecules into organized crystalline structures. Such a hindrance was highest in the case of the PLA-ST-C93A composite because of the high level of compatibility between two phases, as observed in the SEM image [Fig. 3(e)]. As a result, the cold crystallization process gets noticeably suppressed in the PLA-ST-C93A composite and hence the melting enthalpy.

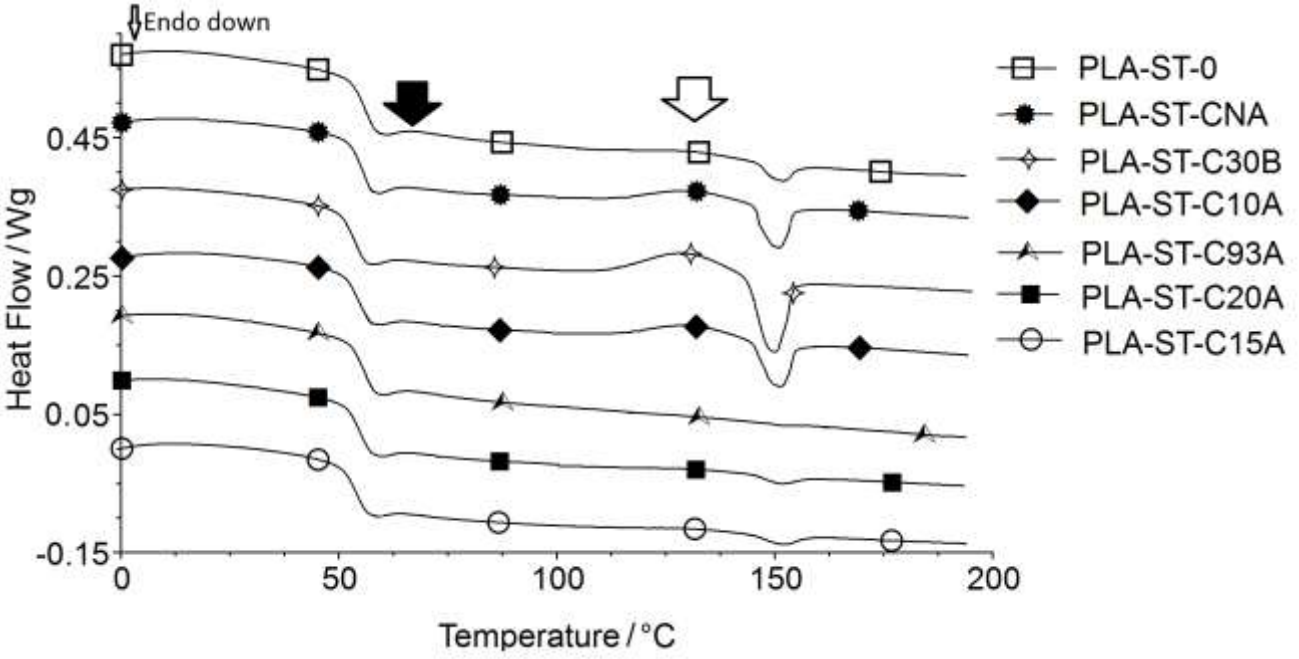

Fig. 4. DSC thermograms of PLA/butylated starch blend and blend/MMT composites with MMT clays of different hydrophobicity. The samples had a clay and starch content of 4.5 wt% and 25.5 wt% of the total composite weight, respectively. The control sample PLA-ST-0 had no clay. The curves were vertically offset for clarity.

To analyze the overlapping transitions of cold crystallization and melting, MDSC has been employed. MDSC enabled a more accurate elucidation of the quantitative results of the glass transition, cold crystallization and melting. For all of the samples, the MDSC thermograms showed that the glass transition observed in the total heat flow [Fig. 5(a)] consisted of a clear glass transition and an enthalpy relaxation. The separation of the thermodynamic and kinetic components ensured that the glass transition associated with the change of specific heat capacity (C_p) appeared as a reversible phenomenon [Fig. 5(b)] and enthalpy relaxation as a non-reversal phenomenon [Fig. 5(c)]. The glass transition temperature (T_g) and associated change in C_p were estimated from the reversible heat flow and summarized in Table 2. It is clear that the composites with moderate to very hydrophobic clays (PLA-ST-C10A, PLA-ST-C93A and PLA-ST-C20A) had marginally higher T_g, although the change in C_p remained unaltered (Table 2). The enthalpy relaxation temperature (T_e) and associated change in enthalpy (ΔH_e) are tabulated in Table 3. The enthalpy relaxation gets retarded in the composites based on moderate hydrophobic to

hydrophobic clays and especially in the PLA-ST-C93A composite when compared with the other composites and even the control sample. This further indicated that the presence of hydrophobic clay in the PLA-ST-C93A composite has reduced the mobility of the PLA chains in the amorphous proportion. It is now important to determine how the W_{af} and W_{raf} change with the hydrophobicity of the clays. The W_{af} and W_{raf} were estimated from Equations 1 and 2, respectively, and the calculated values are presented in the Table 4.

Table 2. Reversing heat flow modulated DSC parameters of PLA/butylated starch blend and blend/MMT composites with clays of different hydrophobicity

Sample	T_g /℃	C_p /J.g^{-1}.℃
PLA-ST-0	56.5 ± 0.1	0.26 ± 0.02
PLA-ST-CNA	57.0 ± 0.6	0.23 ± 0.01
PLA-ST-C30B	55.0 ± 0.2	0.24 ± 0.01
PLA-ST-C10A	58.3 ± 0.2	0.26 ± 0.05
PLA-ST-C93A	58.1 ± 0.9	0.20 ± 0.04
PLA-ST-C20A	58.2 ± 1.4	0.21 ± 0.03
PLA-ST-C15A	57.0 ± 2.6	0.21 ± 0.03

T_g and C_p are the glass transition temperature and the heat capacity change during glass transition, respectively.

Table 3. Non-reversing heat flow modulated DSC parameters of PLA/butylated starch blend and blend/MMT composites with clays of different hydrophobicity

Sample	T_e /℃	ΔH_e /J.g^{-1}	T_{cc} /℃	ΔH_{cc} /J.g^{-1}	T_{mnr} /℃	ΔH_{mnr} /J.g^{-1}
PLA-ST-0	55.3 ± 0.1	1.24 ± 0.02	115.5 ± 0.3	21.39 ± 0.20	147.5 ± 0.6	21.17 ± 0.50
PLA-ST-CNA	55.8 ± 0.5	1.07 ± 0.01	112.1 ± 0.6	21.93 ± 0.57	153.0 ± 0.4	19.11 ± 0.91
PLA-ST-C30B	53.6 ± 0.2	1.15 ± 0.01	110.1 ± 0.1	22.29 ± 0.06	152.4 ± 0.1	18.80 ± 0.57
PLA-ST-C10A	56.2 ± 1.4	1.12 ± 0.22	116.3 ± 0.8	24.18 ± 2.64	148.7 ± 0.9	15.66 ± 1.13
PLA-ST-C93A	56.9 ± 0.9	1.21 ± 0.01	125.2 ± 0.3	2.94 ± 1.01	150.4 ± 0.3	3.44 ± 0.07
PLA-ST-C20A	55.6 ± 0.5	1.12 ± 0.00	122.9 ± 1.2	13.12 ± 0.40	149.8 ± 0.2	14.79 ± 0.11
PLA-ST-C15A	55.2 ± 1.9	1.03 ± 0.09	121.8 ± 1.3	15.87 ± 1.77	152.3 ± 0.7	15.09 ± 1.52

T_e, ΔH_e, T_{cc}, ΔH_{cc}, T_{mnr}, ΔH_{mnr} are the enthalpy relaxation temperature, enthalpy change during enthalpy relaxation, cold crystallization temperature, enthalpy change during cold crystallization, melting temperature for non-reversing heat flow and melting enthalpy change for non-reversing heat flow, respectively.

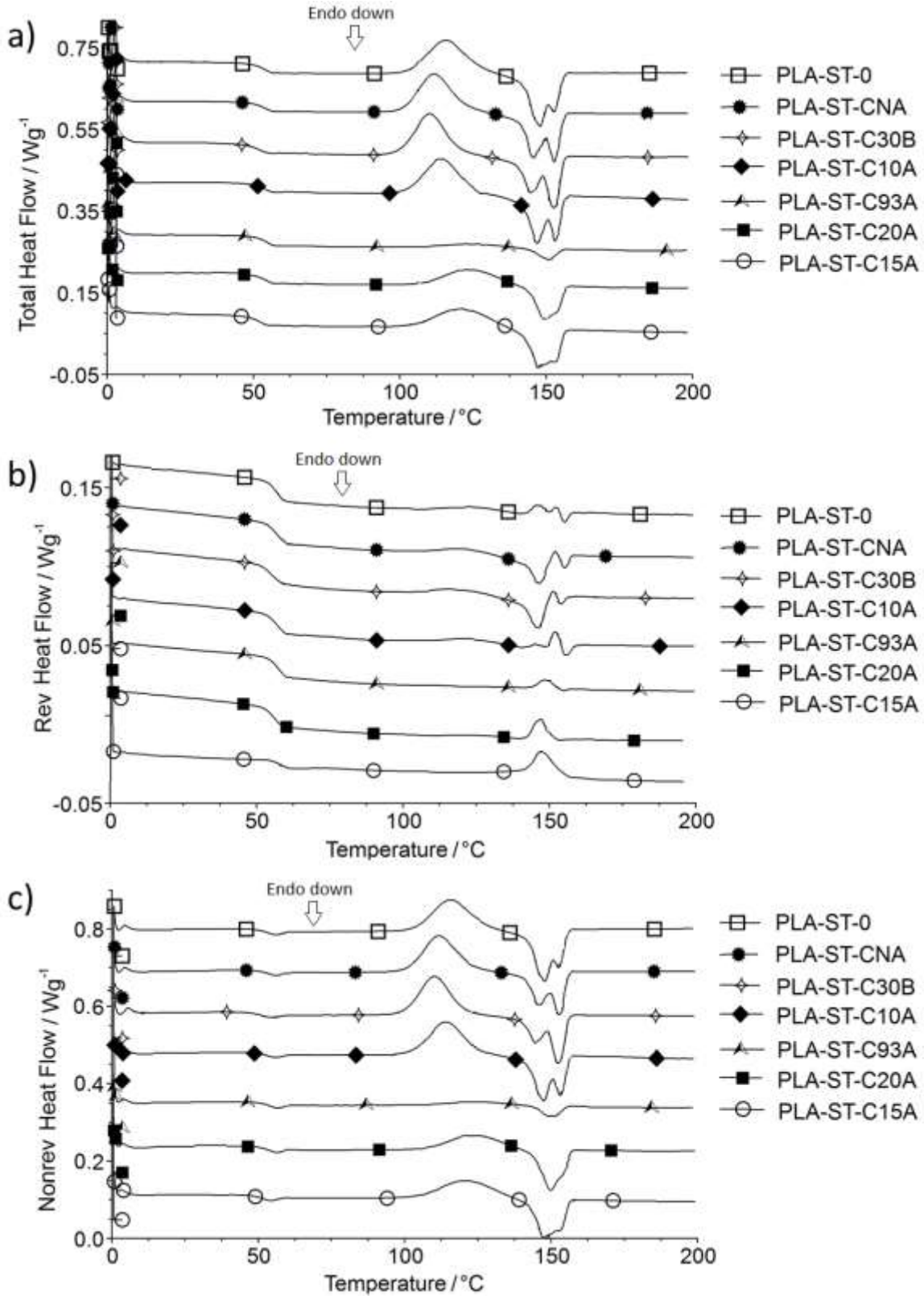

Fig. 5. Modulated temperature DSC thermograms of PLA/butylated starch blend and blend/MMT composites with different degrees of hydrophobicity showing (a) total, (b) reversing and (c) non-reversing heat flows.

Indeed, there was a decrease in the W_{af} in the PLA-ST-clay composites with increasing hydrophobicity of the clay. After the hydrophobic clay-containing sample, there was almost no change in the W_{af} for the composites with very to extremely hydrophobic clays (Table 4). Relative to the control sample, the PLA molecules in the composites with intermediate to extremely hydrophobic clays were less mobile (Table 4). The PLA molecules in the amorphous phase of the composites with the least hydrophobic clays were much more mobile (Table 4).

Table 4. The crystalline, mobile and rigid amorphous phase fractions of PLA/butylated starch blend and blend/MMT composites with clays of different hydrophobicity

Sample	W_{af}	W_{raf}
PLA-ST-0	0.37 ± 0.04	0.59 ± 0.04
PLA-ST-CNA	0.33 ± 0.01	0.62 ± 0.02
PLA-ST-C30B	0.35 ± 0.01	0.61 ± 0.01
PLA-ST-C10A	0.30 ± 0.02	0.62 ± 0.01
PLA-ST-C93A	0.30 ± 0.03	0.66 ± 0.04
PLA-ST-C20A	0.31 ± 0.04	0.64 ± 0.04
PLA-ST-C15A	0.30 ± 0.04	0.63 ± 0.03

W_{af} and W_{raf} are the mobile and rigid amorphous phases, respectively, determined from the C_p values at the glass transition.

As expected, the opposite trend can be observed in the case of W_{raf}. The W_{raf} of the composites with highly hydrophilic to moderate hydrophobic clays or with hydrophobic to extremely hydrophobic clays was slightly higher than that of the control sample (Table 4). On the other hand, the PLA-ST-C93A composite with hydrophobic clay (C93A) tended to have the highest W_{raf}, compared with the less and more hydrophobic clay-containing composites (Table 4). These results indicated that the hydrophobic silicate layers in the PLA-ST-C93A composite probably increased the energy barrier to the PLA molecular mobility.

In summary, the restriction on the PLA chain mobility in the composites with varying hydrophobicity of the clays can be ranked with respect to the hydrophobicity of the clays in the order: hydrophobic clay > from very to extremely hydrophobic clays > hydrophilic to intermediate hydrophobic clays and control sample. This order was also observed at higher temperatures for

both the cold crystallization [Fig. 5(b) and Table 3] and melting phenomena [parts (a), (b) and (c) of Fig. 5 and Tables 2 and 3]. Usually, cold crystallization appears in a non-reversible heating cycle. Increase in temperature beyond T_g sometimes allows polymer chains to undergo further chain rearrangement, which results in the appearance of exothermic peaks during heating; this is known as cold crystallization. In the present study, a sharp cold crystallization peak can be observed for the control sample, as well as in the composites based on CNA, C30B and C10A. The cold crystallization peak almost diminished in the PLA-ST-C93A composite and reappeared again in the composites based on C20A and C15A. Table 3 supports this observation. The highest shift in the cold crystallization temperature (T_{cc}) occurred in the PLA-ST-C93A composite. Due to the higher value of the rigid amorphous fraction (Table 4), it was difficult for the polymer chains to undergo the cold crystallization process earlier. The enthalpy of cold crystallization (ΔH_{cc}) is extremely low for this sample. However, further heating results in some reversible chain rearrangement during melting, and the melting phenomenon can be observed in the non-reversible cycle. Like T_{cc}, the non-reversible melting temperature (T_{mnr}) also shifted towards the high temperature. The enthalpy of non-reversible melting (ΔH_{mnr}) followed the same trend as ΔH_{cc} in the case of the PLA-ST-C93A composite. In the case of the control and composites with CNA, C30B and C10A, it is interesting to note that the melting process is quite complex. It comprises a sharp, non-reversible melting along with a continuous reversible melting and chain rearrangement. This behavior changes in very to extremely hydrophobic clay-based systems. Reversible chain rearrangement is dominant there instead of reversible melting. For those samples, the melting mainly appeared as a non-reversible phenomenon.

The incidence of the exothermic transition during melting was consistent with the observations from both TEM and SEM, which showed that the composites with the hydrophobic to extremely hydrophobic clays tended to have less intimate interphase boundaries when compared with those with CNA, C30B or C10A containing composites. Therefore, the exotherms observed in the

composites with C93A, C20A and C15A could have resulted from entropic adjustment at the interphase boundary to form more stable structures for the composites. Because the composites with the hydrophilic to moderate hydrophobic clays and the control sample had more distinct boundaries, the endotherms observed could indicate a collapse in the boundary structures in these composites. Moreover, neither prominent double melting peaks nor exotherm peaks were observed for the composite with C10A, which has a structure similar to the PLA-ST-C30B composite. It is possible that another factor plays a major role rather than the presence of delaminated silicate layers at the interphase.

When the intercalated silicate layers were mostly located within the starch phase (except C20A) and at the interphase boundary, a common intercalated interphase boundary structure plays an important role rather than an exfoliated or delaminated boundary structure. In a common intercalated structure, the two polymer molecules are held in the inter-silicate layer space tightly. On the other hand, a delaminated boundary would have molecules of PLA mingling with starch molecules and clay platelets without the confinement accorded by the inter-silicate layer space as for intercalated structures. The common intercalation of both PLA and starch in the clay gallery would lead to less mobility of the PLA molecules in the intercalated structure. This explains why the mobile amorphous fraction is lowest in the PLA-ST-C93A composite.

4.3. Isothermal crystallization kinetics

Several criteria are prerequisites for appropriate utilization of the Avrami model [29-31]. Among the criteria are: no change in the sample volume during crystallization, a constant crystal growth rate, a unique crystal nucleation that is either thermal or athermal and a constant crystal shape type during growth. Irrespective of these several criteria, among others, the Avrami model has been widely utilized for bulk crystallization analysis [34, 35]. It was used in the present study with an assumption that the conditions for its utilization are at least approximately met by the PLA/ butylated starch/clay composite systems.

In the Avrami model [29-31], the bulk crystallization kinetics of crystalline polymer entities from their polymer melts are assessed based on the development of the crystalline fraction (X_t) of the material with time. According to the model:

$$X_t = 1 - e^{-kt^n} \qquad (3)$$

where X_t is the crystalline fraction at time *t*, and *k* and *n* are the Avrami bulk crystallization constant and exponent, respectively.

The heat flow versus time plots for the PLA-ST blend and PLA-ST-clay composites with different hydrophobicity are shown in Fig. 6. All of the samples showed an increase in heat flow as the crystallization proceeded until a peak value, after which the heat flow reduced until the base line was recovered. The maximum heat flow peaks of the samples with least hydrophobic and extremely hydrophobic clay containing blend composites occurred to the left of that of the control sample , while those of the composites with moderate to very hydrophobic clays shifted to the right.

The total crystallization times of the composites with the relatively least hydrophobic and extremely hydrophobic clays had lower total crystallization times than the control sample. On the other hand, the total crystallization time of the composites of moderate to very hydrophobic clays had longer total crystallization times compared with the control sample. The total crystallization times (points where the baseline was recovered) were approximately 400, 225, 250, 550, 800, 550 and 275 min for the control sample and the composites with CNA, C30B, C10A, C93A, C20A and C15A, respectively. The composite systems with the moderate to very hydrophobic clays required more time for complete crystallization compared with the control sample, while the required time reduced in the case of less hydrophobic and very hydrophobic clays. This trend was probably due to the reduced mobility of the PLA molecules, as indicated in Table 4.

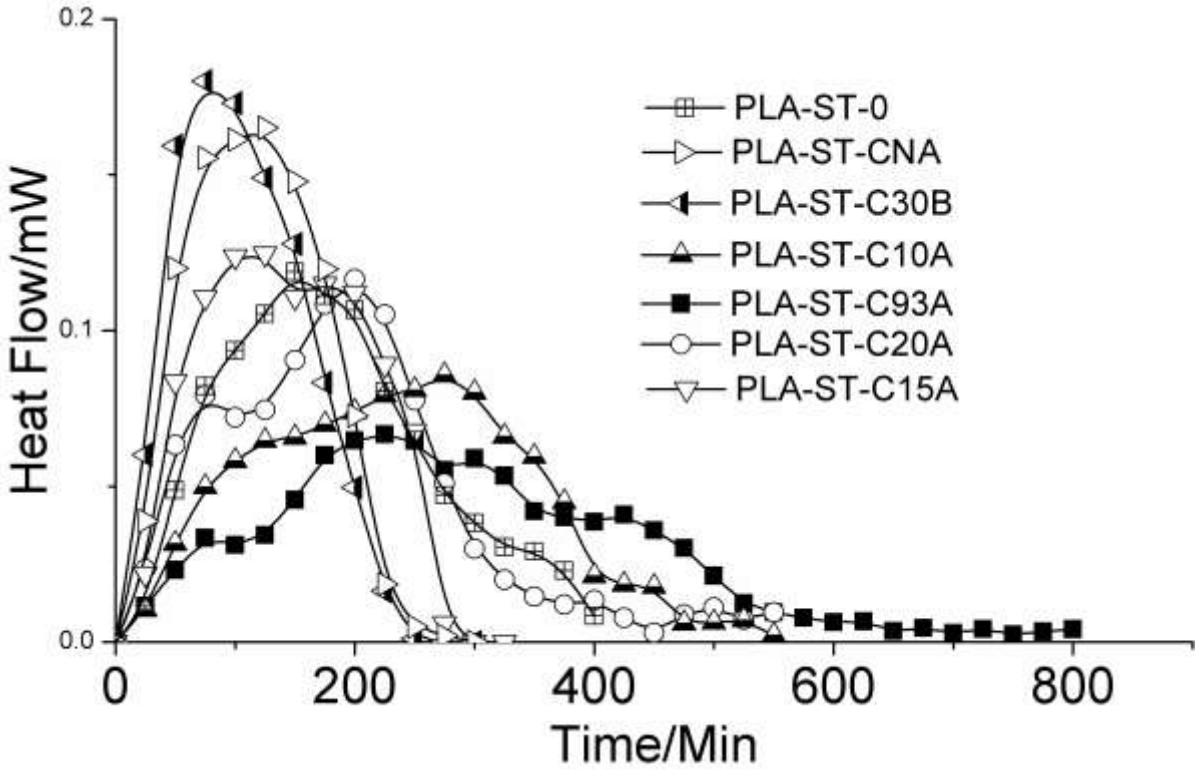

Fig. 6. Heat flow versus time plots for PLA/butylated starch blend and blend/clay composites with clays of different hydrophobicity held isothermally at 120°C.

The trend in the total heat requirement for crystallization was also illustrated by the plot of the crystalline proportion (X_t) versus time (t) (Fig. 7). There were shifts in the curves to the left and right of the control sample without any added clay, as observed with the heat flow *vs.* time curves. The $t_{1/2}$ was determined directly from the plots of relative crystallinity *vs.* time according to Siqueira et al. [36]. The $t_{1/2}$ values were 158, 104, 89, 223, 269, 172 and 133 min for the control sample and composites with CNA, C30B, C10A, C93A, C20A and C15A, respectively.

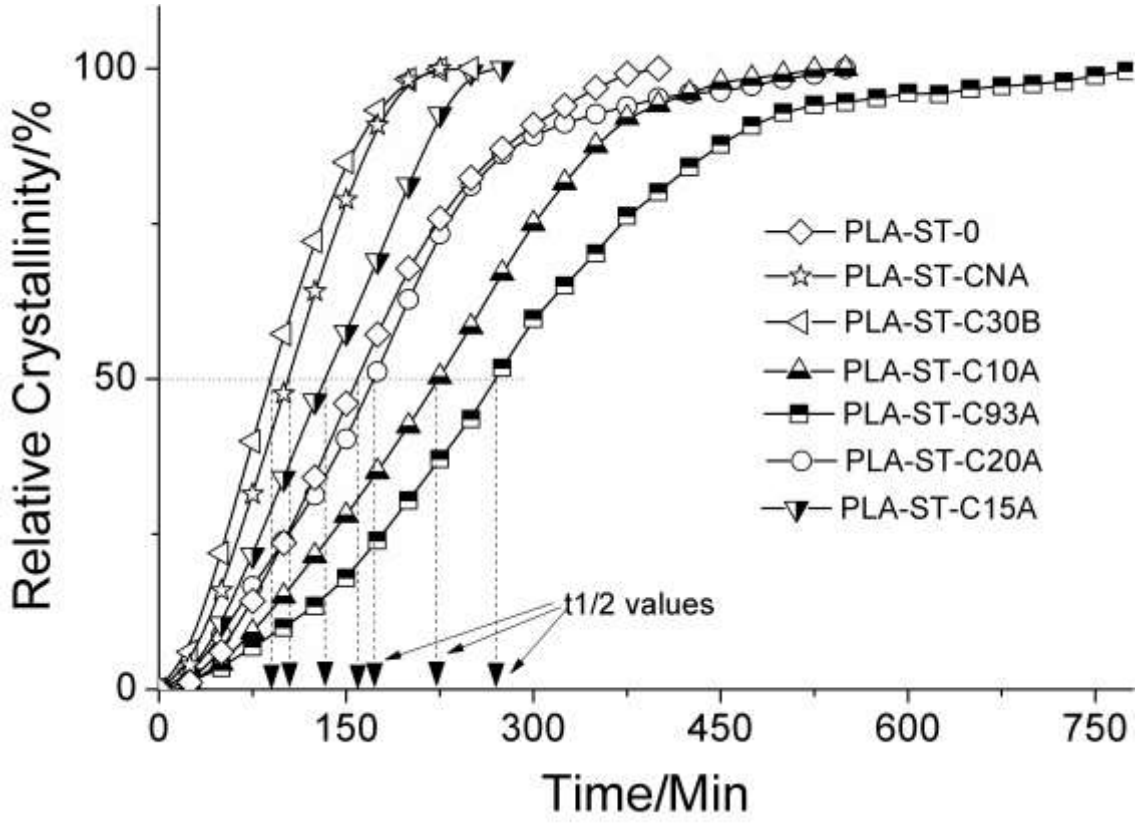

Fig. 7. Relative crystallinity as a function of time for PLA/butylated starch blend and blend/clay composites with clays of different hydrophobicity held isothermally at 120°C.

To obtain the *n* and *k* Avrami model parameters, a plot of ln [-ln(1-X_t)] versus ln (*t*) is used. Fig. 8 shows the Avrami ln [-ln(1-X_t)] versus ln (*t*) plot for the PLA/butylated starch composites with clays of different hydrophobicity. The values of *k* and *n* are obtained from linear fitted data (Fig. 8) as the intercept and gradient, respectively. Table 5 presents the Avrami model analysis parameters. The obtained R^2 values were at least 0.99, which indicated a reasonably good fit of the data to the model. Usually, only one of the Avrami bulk analysis parameters can generate sufficient information to understand the isothermal bulk crystallization process.

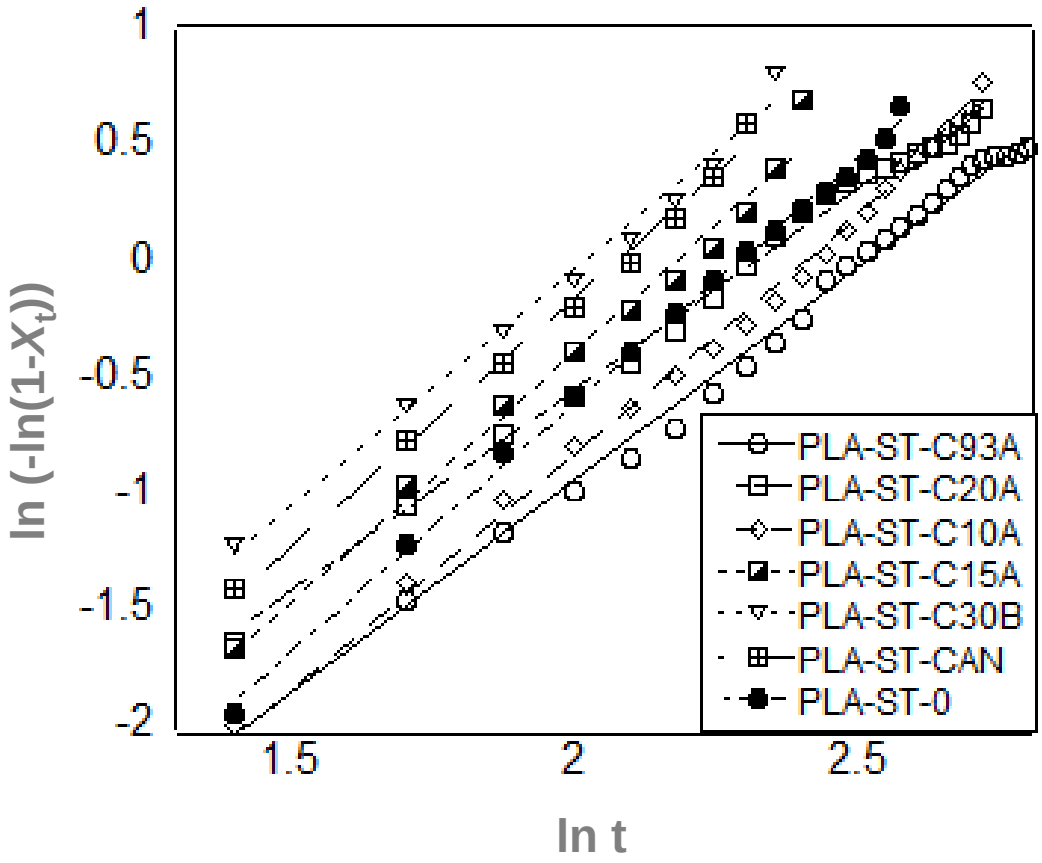

Fig. 8. Avrami plots for PLA-ST-clay composites with clays of different degrees of hydrophobicity held isothermally at 120°C.

Table 5. Isothermal crystallization Avrami parameters of PLA-ST blend and PLA-ST-clay composites with clays of different hydrophobicity held isothermally at 120°C for 4 h.

Sample	Avrami model parameters		
	n	ln *k*	R^2
PLA-ST-0	2.12 ± 0.02	-4.84 ± 0.06	0.99889
PLA-ST-CNa	2.13 ± 0.07	-4.40 ± 0.14	0.99691
PLA-ST-C30B	2.05 ± 0.08	-4.08 ± 0.16	0.99485
PLA-ST-C10A	2.03 ± 0.03	-4.90 ± 0.08	0.99753
PLA-ST-C93A	1.83 ± 0.03	-4.59 ± 0.07	0.99685
PLA-ST-C20A	1.92 ± 0.03	-3.99 ± 0.07	0.99694
PLA-ST-C15A	2.16 ± 0.10	-4.69 ± 0.21	0.99162

The Avrami exponent (*n*-value) is an indicator of the nucleation type and growth geometry. Values of *n* that range from 1-4 indicate a non-inhibited, three-dimensional spherulite, while values ranging from 3-4 indicate inhibited, two-dimensional spherulite growths. The values of the Avrami

exponent that range from 1-2 have been attributed to athermal or thermal nucleation in disc-shaped geometries, with the rate-determining phenomenon being either nucleation or diffusion [37]. The spherulites in the present study were therefore flat/disc shaped and grew through athermal or thermal nucleation.

From Table 5, it can be observed that the exponent value decreased with increased clay hydrophobicity until the composites with C93A and then increased thereafter until PLA-ST-C15A, which has extremely hydrophobicity (Table 1). The trend in the Avrami exponent values was in accordance with the results of the mobile and rigid amorphous phase proportions summarized in Table 4. Although *k* gives a measure of the amount and type of nucleation and shape of the spherulites, there was apparently no clear trend in the *k* values (Table 5).

4.4. POM observation

POM experiments were conducted to obtain a more accurate assessment of the spherulite growth rate. Moreover, a microscopic evaluation is necessary to validate the conclusions made from the Avrami model analysis. The spherulite morphology of PLA spherulites in the PLA-ST blend and PLA-ST-clay composites is shown in Fig. 9. For all of the samples, the spherulite populations consisted of only one spherulite type (regular circular with similar radius), which indicated that the nucleation was athermal. This observation confirmed the athermal nucleation in all samples based on the Avrami exponent values obtained (approximately in the range of 1 to 2, Table 5).

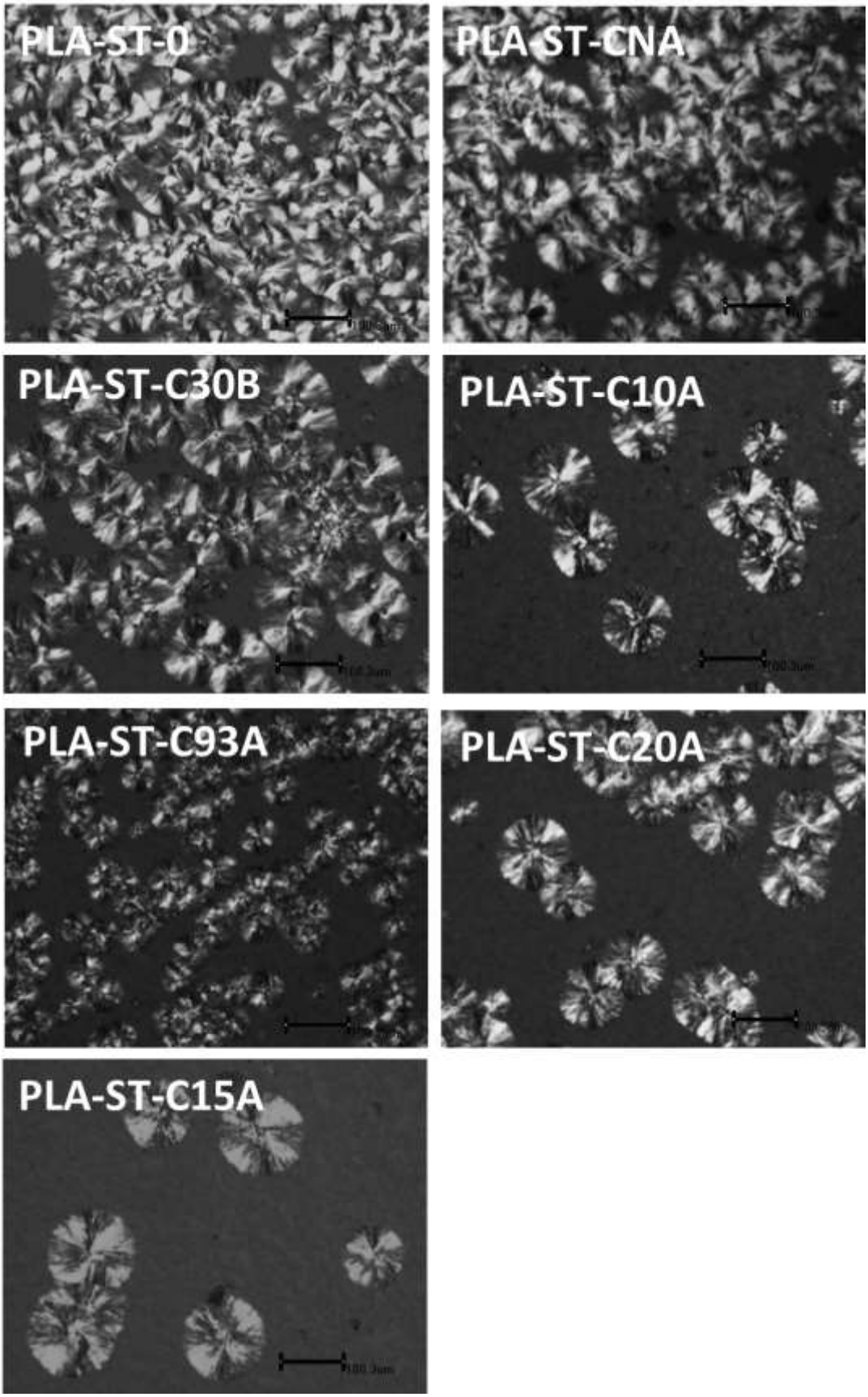

Fig. 9. POM images of PLA-ST blend and PLA-ST-clay composites with clays of different degrees of hydrophobicity held isothermally at 120°C; the reported images were taken after 80 min. The black line at the bottom right corner of each image is the scale bar of 100.3 μm.

The number of spherulites per unit area was clearly higher in the PLA-ST-clay composites with CNA, C30B, C93A and the control sample when compared with those of C10A, C20A and C15A. This indicated that the sites for primary nucleation were more in the former group compared with the latter group. This trend was in accordance with that of the TEM results, which showed that the composites with C10A, C20A and C15A had a partially agglomerated/intercalated, intercalated and highly delaminated structure, while those with C93A, C30B and CNA were either common intercalated or had an aggregated (CNA) structure with very few silicate layers at the interphase. The primary nucleation was therefore related to the composite structure. Primary nucleation, when compared with secondary nucleation, requires a larger amount of specific area to attain the critical nucleus radius required to overcome the free energy barrier to crystallization [38].

4.5. Crystal growth rate

The spherulite growth rate (*G*) [34, 35] of the neat blend and composites with different clays is shown in Table 6. The R^2 values for the linearity of the growth rate were >0.95, which indicated that the spherulite growth was linear, a condition necessary for the validity of the Avrami model analysis. A higher spherulite growth relative to the control sample was observed in the composites with CNA, C30B, C10A, C20A and C15A. The composites with C93A, on the other hand, had a significantly lower spherulite growth rate than that of the control sample.

Table 6. Crystalline spherulite growth rate (G) of PLA/butylated starch blend and blend/clay composites with different clays of different degrees of hydrophobicity crystallized isothermally at 120°C for 80 min.

Sample	Spherulite growth rate (*G*), (μm/min)	R^2
PLA-ST-0	0.90 ± 0.10	0.987
PLA-ST-CNA	1.15 ± 0.03	0.952
PLA-ST-C30B	1.24 ± 0.02	0.982
PLA-ST-C10A	1.12 ± 0.19	0.985
PLA-ST-C93A	0.58 ± 0.16	0.976
PLA-ST-C20A	1.08 ± 0.09	0.977
PLA-ST-C15A	1.33 ± 0.03	0.982

The spherulite growth rate increased thereafter with composites processed from very to extremely hydrophobic clays. These results are consistent with the trend in the DSC mobile and rigid amorphous phase data and with the $t_{1/2}$ values obtained from the crystal fraction *vs.* time plots. This implied that the PLA molecules were relatively less mobile in the composites with C93A, while they were more mobile in the composites processed with other clays.

Qualitatively, it was observed that the composite with C93A has much smaller spherulites compared with the other samples. Smaller spherulites lead to materials with better mechanical properties, such as elongation at break and moduli, when compared with those with larger spherulites. The composites with C93A would probably have improved mechanical properties compared with those with CNA, C30B, C10A, C20A and C15A due to matching of its hydrophobicity with that of the butylated starch phase. We will report concerning this in our upcoming article.

5. Conclusions

The objective of this work was to study the effect of the addition of nanoclays with varying hydrophobicity on the structure, morphology and thermal properties of PLA/butylated-starch/nanoclay ternary composites. The structural analysis using TEM showed that silicate layers were mostly intercalated and preferably located in the starch phase and at the interphase, as expected, in very hydrophobic nanoclay containing-blend composite. This was attributed to the balance of hydrophilicity/hydrophobicity and interlayer spacing of nanoclay. The morphological studies indicated that a match in hydrophobicity between the nanoclay surface and that of the dispersed phase is necessary to have a composite with finer morphology. This indicates that a requisite hydrophobicity is needed to have common intercalation of both polymers at the interface. As the hydrophobicity of the added nanoclay tends toward that of the dispersed, less hydrophobic butylated starch phase, there are significant changes in the thermal properties and bulk

crystallization behavior. Although there is a tendency to have a lower PLA molecular mobility and reduced spherulite growth rates as the added nanoclay hydrophobicity tends toward intermediate from low and relatively high, the blend composite processed with hydrophobic nanoclay (C93A) has much smaller spherulites compared with other samples. Therefore, we may expect that this composite will show a balance of mechanical and other properties, and a study of the relationship between morphology and mechanical properties is ongoing in our laboratory; we will report separately. This study has therefore clearly shown the qualitative relation of the nanoclay hydrophobicity with the phase morphology and thermal properties of blend composites.

Acknowledgments

The authors would like to thank the Department of Science and Technology and the Council for Scientific and Industrial Research for their financial support. We would also like to thank Dr. Lumbizani Moyo for helping in the cryo-sectioning of samples for TEM analysis.

References

[1] Ray SS. Polylactide-based bionanocomposites: a promising class of hybrid materials. Acc Chem Res 2012; 45:1710−20.

[2] Ojijo V, Ray SS. Processing strategies in bionanocomposites. Prog Polym Sci 2013; 38:1543−89.

[3] Copeland L, Blazek J, Salman H, Tang MC. Form and functionality of starch. Food Hydrocolloids 2009; 23:1527−34.

[4] Rahmat AR, Rahman WAWA, Sin LT, Yussuf AA. Approaches to improve compatibility of starch filled polymer system: a review. Mater Sci Eng C 2009;29:2370−7.

[5] Wokadala OC, Emmambux NM, Ray SS. Inducing PLA/starch compatibility through butyl-etherification of waxy and high amylose starch. Carbohyd Polym 2014;112:216−24.

[6] Raquez JM, Nabar Y, Narayan R, Dubois P. In situ compatibilization of maleated thermoplastic starch/polyester melt-blends by reactive extrusion. Polym Eng Sci 2008; 48:1747−54

[7] Raquez JM, Nabar Y, Narayan R, Dubois P. Preparation and characterization of maleated thermoplastic starch-based nanocomposites. J Appl Polym Sci 2011;122:639−47.

[8] Dubois P, Narayan R. Biodegradable compositions by reactive processing of aliphatic polyester/polysaccharide blends. Macromol Symp 2003;198:233−43.

[9] Ray SS, Pouliot S, Bousmina M, Utracki LA. Role of organically modified layered silicate as an active interfacial modifier in miscible polystyrene/polypropylene blends. Polymer 2004; 45:8403−13.

[10] Ray SS, Bousmina M. Compatibilization efficiency of organoclay in an immiscible polycarbonate/poly(methyl methacrylate) blend. Macromol Rapid Commun 2005;26:450−5.

[11] Hong JS, Namkung H, Ahn KH, Lee SJ, Kim C. The role of organically modified layered silicate in the breakup and coalescence of droplets in PBT/PE blends. Polymer 2006;47:3967−75.

[12] Martins C, Larocca N, Paul D, Pessan L. Nanocomposites formed from polypropylene/EVA blends. Polymer 2009;50:1743−54.

[13] Ray SS, Bandyopadhyay J, Bousmina M. Effect of organoclay on the morphology and properties of poly(propylene)/poly[(butylene succinate)-co-adipate] blends. Macromol Mater Eng 2007;292:729−47.

[14] Wu D, Zhang Y, Zhang M, Yu W. Selective localization of multiwalled carbon nanotubes in poly(ε-caprolactone)/polylactide blends. Biomacromolecules 2009;10:417−424.

[15] Wu D, Lin D, Zhang J, Zhou W, Zhang M, Zhang Y, Wang D, Lin B. Selective localization of nanofillers: effect of morphology and crystallization on PLA/PCL blends. Macromol Chem Phys 2011;212:613−26.

[16] Chen G.-X, Kim HS, Kim ES, Yoon JS. Compatibilization-like effect of reactive organoclay on the poly(L-lactide)/poly(butylene succinate) blends. Polymer 2005; 46: 11829−36.

[17] Chen GX, Yoon JS. Morphology and thermal properties of poly(L-lactide)/poly(butylene succinate-co-butylene adipate) compounded with twice functionalized clay. J Polym Sci Part B Polym Phys 2005; 43: 478−87.

[18] As'habi L, Jafar SH, Khonakdar HA, Boldt R, Wagenknecht U, Heinrich G. Tuning the processability, morphology and biodegradability of clay incorporated PLA/LLDPE blends via selective localization of nanoclay induced by melt mixing sequences. eXPRESS Polym Letts 2013; 7:21−39.

[19] Ojijo V, Cele H, Ray SS. Morphology and properties of polymer composites based on biodegradable polylactide/poly[(butylene succinate)-co-adipate] blend and nanoclay. Macromol Mater Eng 2011;296:865−77.

[20] Ojijo V, Malwela T, Ray SS, Sadiku R. Unique isothermal crystallization phenomenon in the ternary blends of biopolymerspolylactide and poly[(butylene succinate)-co-adipate] and nano-clay. Polymer 2012; 53:505−18.

[21] Ojijo V, Ray SS, Sadiku R. Effect of nanoclay loading on the thermal and mechanical properties of biodegradable polylactide/poly[(butylene succinate)-co-adipate] blend composites. ACS Appl Mater Interfaces 2012; 4:2395−405.

[22] Gao Y, Dai Y, Zhang H, Diao E, Hou H, Dong H. Effects of organic modification of montmorillonite on the performance of starch-based nanocomposite films. Appl Clay Sci 2014;99:201−6.

[23] Bien F, Wiege B, Warwel S. Hydrophobic modification of starch by alkali-catalyzed addition of 1,2-epoxyalkanes. Starch-Stärke 2001;53:555−9

[24] Van Krevelen DW. Properties of Polymers, 4th Ed. Amsterdam: Elsevier, 1990.

[25] Righetti MC, Tombari E, Angiuli M, Lorenzo MLD. Enthalphy based determination of crystalline, mobile amorphous and rigid amorphous fractions in semicrystalline polymers: poly(ethylene terephthalate). Thermochimica Acta 2007;462:15−24.

[26] Iannace S, Nicolais L. Isothermal crystallization and chain mobility of poly(L-lactide). J Appl Polym Sci 1997;64:911−9.

[27] Zuza E, Ugartemendia JM, Lopez A, Meaurio E, Lejardi A, Sarasua J-R. Glass transition behavior and dynamic fragility in polylactides containing mobile and rigid amorphous fraction. Polymer 2008;49:4427−32.

[28] Magoń A, Pyda M. Study of crystalline and amorphous phases of biodegradable poly(lactic acid) by advanced thermal analysis. Polymer 2009;50:3967−73.

[29] Avrami M. Kinetics of phase change. I general theory. J Chem Phys 1939;7:1103−12.

[30] Avrami M. Kinetics of phase change. II transformation-time relations for random distribution of nuclei. J Chem Phys 1940;8:212−24.

[31] Avrami M. Granulation, phase change, and microstructure kinetics of phase change. III. J Chem Phys 1941;9:177−84.

[32] Ray SS, Yamada K, Okamoto M, Fujimoto Y, Ogami A, Ueda K. New polylactide/layered silicate nanocomposites. 5. Designing of materials with desired properties. Polymer 2003;44:6633−46.

[33] Bandyopadhyay J, Ray SS, Scriba M, Wesley-Smith J. A combined experimental and theoretical approach to establish the relationship between shear force and clay platelet delamination in melt-processed polypropylene nanocomposites. Polymer 2014; 55: 2233–45.

[34] Ray SS. Clay-containing polymer nanocomposites: from fundamental to real applications. Amsterdam: Elsevier; 2013.

[35] Ray SS. Environmentally-friendly polymer nanocomposites: types, processing and properties. London: Woodhead Publishing; 2013.

[36] Siqueira G, Fraschini C, Bras J, Dufresne A, Prud'homme R, Laborie M-P. Euro Polym J 2011;47:2216−27

[37] Hiemenz PC. Polymer chemistry: The Basic Concepts: CRC press, 1984.

[38] Wunderlich BW. Macromolecular Physics, Vol. 2, Elsevier: New York 1976.